Astron. Astrophys. 349, 751–764 (1999)

ASTRONOMY AND ASTROPHYSICS

IR colors and sizes of faint galaxies⋆

P. Saracco[1], **S. D'Odorico**[2], **A. Moorwood**[2], **A. Buzzoni**[1], **J.-G. Cuby**[3], **and C. Lidman**[3]

[1] Osservatorio Astronomico di Brera, via E. Bianchi 46, I-22055 Merate (LC), Italy
[2] European Southern Observatory, ESO, Karl-Schwarzschild-Strasse 2, D-85748 Garching bei München, Germany
[3] European Southern Observatory, ESO, Casilla 19001, Santiago 19, Chile

Received 19 April 1999 / Accepted 3 August 1999

Abstract. We present J and Ks band galaxy counts down to J=24 and Ks=22.5 obtained with the new infrared imager/spectrometer, SOFI, at the ESO New Technology Telescope. The co-addition of short, dithered, images led to a total exposure time of 256 and 624 minutes respectively, over an area of ~ 20 arcmin^2 centered on the NTT Deep Field. The total number of sources with S/N> 5 is 1569 in the J sample and 1025 in the Ks-selected sample. These are the largest samples currently available at these depths. A d$logN$/dm relation with slope of ~ 0.36 in J and ~ 0.38 in Ks is found with no evident sign of a decline at the magnitude limit. The observed surface density of "small" sources is much lower than "large" ones at bright magnitudes and rises more steeply than the large sources to fainter magnitudes. Fainter than $J \sim 22.5$ and Ks~ 21.5, small sources dominate the number counts. Galaxies get redder in J-K down to J~ 20 and Ks~ 19. At fainter magnitudes, the median color becomes bluer with an accompanying increase in the compactness of the galaxies. We show that the blue, small sources which dominate the faint IR counts are not compatible with a high redshift ($z > 1$) population. On the contrary, the observed color and compactness trends, together with the absence of a turnover at faint magnitudes and the dominance of small sources, can be naturally explained by an increasing contribution of sub-L^* galaxies when going to fainter apparent magnitudes. Such evidence strongly supports the existence of a steeply rising ($\alpha \ll -1$) faint end of the local infrared luminosity function of galaxies - at least for luminosities $L < 0.01L^*$.

Key words: cosmology: observations – galaxies: evolution – galaxies: luminosity function, mass function – galaxies: photometry – galaxies: statistics – infrared: galaxies

1. Introduction

Near infrared (IR) selected samples may provide significant advantages over optically selected samples in studying galaxy evolution due to the small and almost galaxy type independent k-corrections at these wavelengths (Cowie et al. 1994). Moreover, IR selection provides samples which are not biased towards star-forming galaxies and may trace the mass of the galaxies over a wide range of redshift. For these reasons, since the beginning of nineties, near IR galaxy counts have been considered a powerful cosmological test. This, however, was discovered not to be the case when it was realized that deep optical and near IR observations were difficult to reconcile without assuming an *ad hoc* population of galaxies or extreme merging scenario (Cowie et al. 1990; Babul & Rees 1992; Broadhurst et al. 1992; Gronwall & Koo 1995; Yoshii & Peterson 1995). Moreover, the large uncertainty on the slope of the faint-end tail of the local LF, especially in the near IR, means that the hypothesis on the nature of the very faint population of galaxies is completely unconstrained in terms of redshift and thus in terms of evolution.

The addition of color information to number counts may shed light on the different populations that contribute at a given magnitude and/or the redshift of galaxies beyond the spectroscopic limits (e.g. Lilly et al. 1991).

Some efforts have been made to include in the analysis of faint galaxies also information about the morphological structure derived both from ground based observations (e.g. Lilly et al. 1991; Colless et al. 1994) and, more recently, from HST images.

Morphological classifications based on visual inspection of optical HST images have revealed that the faint field population is apparently dominated by irregular and merging galaxies (Glazebrook et al. 1995a; Driver et al. 1995). However, the comparison of optical images of distant galaxies with possible local counterparts could give misleading results since the surface brightness dimming and the reduced signal-to-noise ratio tend to emphasize high contrast features. Also, as discussed by Abraham et al. (1996), the band-pass shifting effects arising from the k-correction implies that low-redshift optical images are compared with high-redshift UV images which, inevitably, show an increasing irregularity in their morphology.

Most of the uncertainties related to image structure vanish when dealing with near-IR data since they trace the underlying old stellar population of galaxies out to $z \sim$ 3-4.

Recently, Bershady et al. (1998) derived deep near-IR galaxy counts in two high-latitude Galactic fields, summing up to 1.5 arcmin^2, observed with the Keck telescope to depths of J=24.5 and K=24. They find that counts do not roll over by

Send offprint requests to: Paolo Saracco

⋆ Based on observations collected at the European Southern Observatory, La Silla, Chile

K~ 22.5 and that the smallest galaxies dominate at magnitudes fainter than J$\sim$ 23 and K$\sim$ 21.5. They also find no hint of a flattening in the counts at the limits of the survey and mean colors bluer than expected from a no evolution prediction. These features are discussed under the hypothesis of an increasing contribution of sub-L* galaxies at faint magnitudes, i.e. a rising faint end luminosity function (LF), and/or evolution of galaxies.

In this paper we present counts, near-IR colors, sizes and compactness indices of faint galaxies observed at the ESO NTT telescope to depths comparable with the faintest previous ground-based surveys but over a much larger area. In Sect. 2 we describe the observations and the photometric calibration while in Sect. 3 we describe the image processing and analysis and the construction of our photometric sample. In Sect. 4 the differential galaxy counts and colors are derived while in Sect. 5 we describe the method used to estimate the size and compactness of sources and present counts as a function of galaxy size. The discussion of the results is presented in Sect. 6 and Sect. 7 summarizes our results and conclusions.

2. Observations and photometric calibration

The observational data used were obtained during commissioning of the SOFI infrared imager/spectrometer (Moorwood et al. 1998) at the ESO 3.5 m New Technology Telescope (NTT) in March 1998 and are publicly available (http://www.eso.org/science/sofi_deep/). SOFI is equipped with a 1024×1024 pixel Rockwell Hawaii array providing a plate scale of 0.292$\pm$0.001 arcsec/pix in the wide-field observing mode. The total field of view on the sky is thus about 5×5 arcmin per frame. Field center was located at $\alpha = 12^h : 05^m : 26.02^s$, $\delta = -07^o : 43' : 26.43''$ and observations were made in the two near-infrared filters J (λ_c=1.247 μm; $\Delta\lambda \sim 0.290$ μm), and Ks (λ_c=2.162 μm;$\Delta\lambda \sim 0.297$ μm).

The observations were gathered over several nights but under quite homogeneous seeing conditions ranging from 0.6–0.9 arcsec (median FWHM = 0.75 arcsec). The standard jitter technique was used with effective exposure times for each individual frame of 1 min in Ks, (resulting from the average of 6 exposure of 10 s each), and 2 min in J (resulting from the average of 6 exposures of 20 s each).The jitter offsets were controlled by an automated template procedure (the reader is referred to the SOFI User Manual for more details) which was used to randomly offset the telescope position within a box of 40 arcsec on the sky. The deepest exposures were therefore achieved across the central 4.45×4.45 arcmin field. A single measurement normally consisted of 60 and 30 frames in Ks and J, respectively, the whole "duty" cycle amounting to a total of 1 hour integration. These were repeated to achieve total exposure times of 624 min in Ks and 256 min in J in the final co-added images.

Photometric calibration of the observations has been made by observing several standard stars from the list of Infrared NICMOS Standard Stars (Persson et al. 1998). Star magnitudes ranged between $10.8 < Ks < 11.7$ and $11.3 < J < 12.0$, and instrumental total flux has been estimated by deriving the growth curve for each star. This allowed us to achieve a typical uncertainty of ± 0.02 mag in the photometric zero point.

The estimated magnitudes have been then corrected for atmospheric extinction assuming A_{Ks}=0.11 and A_J=0.08.

3. Image processing and analysis

3.1. Flat fielding

Raw frames have been first corrected for the bias pattern by subtracting, for each night, a median dark frame and then flat fielded to correct for pixel-to-pixel gain variations.

Two different types of flat field were compared for each band. A differential dome flat field (DDF), obtained by subtracting lamp-on and lamp-off images of the illuminated dome, and a "superflat" (SF) obtained for each night by combining all the images of the observed field (over 120 frames throughout). Template flat-fields were cleaned of both "hot" and "cold" pixels via the IRAF CCDMASK routine (we adopted a $\pm 6\sigma$ rejection threshold). Rejected pixels were "filled in" by local interpolation on the frame (via the IRAF/FIXPIX routine), and the resulting final flats have been then normalized to their mean value.

Comparison among the different flat fields has been made on the basis of both high- and low-frequency systematics, that is including pixel-to-pixel variations as well as the magnitude scatter of star measurements made on a grid of positions across the field. Having verified that both the DDF and SF flat fields gave comparable results, allowing a magnitude accuracy within ~ 0.02 mag, we decided to adopt the DDF as a fiducial template for our observations.

3.2. Co-addition

After flat fielding and standard sky subtraction, each basic set of frames was registered and finally co-added to produce a single image corresponding to one hour exposure. The whole procedure was accomplished using the original *Jitter* programme by Devillard (1998; http://www.eso.org/eclipse).

For each input frame, the software first generates a sky-subtracted image resulting from filtering a set of typically 10 time-adjacent frames. Frame registering is then performed via cross-correlation among the brightest objects in the fields. A sub-pixel offset accuracy is assured by *Jitter* so that a resampling of the images is also required before the stacking procedure. Co-addition is then performed, adding a filter to remove spurious pixel values before averaging.

Since observations span different nights and were therefore collected under different photometric conditions and airmass, each one hour exposure image, derived from the recombination of the basic set of frames, has been shifted to the same magnitude zero point before co-addition to produce the final image. In order to estimate the flux scaling factor, the instrumental magnitudes of the 20 brightest objects ($14 < Ks <$19; $16 < J < 20$) were compared throughout the frames. The photometric uncertainty introduced by such scaling is about 0.02 mag. Once rescaled,

Table 1. Summary of observations and image quality.

Filter	Number of frames	t_{exp} (s)	$< FWHM >$ (arcsec)	μ mag/arcsec^2	m_{lim} (3σ)
Ks	624	37440	0.75	23.95	22.76
J	128	15240	0.75	25.75	24.57

the 11 Ks frames and the 5 J frames were co-added by *Jitter* without applying any filtering before averaging.

The surface brightness cutoff as well as the 3σ magnitude limit for a $2\times$ FWHM (1.5 arcsec) circular aperture from the co-added Ks and J band frames are reported in Table 1.

3.3. Object detection

Systematic object detection has been performed across the central deepest portion (4.45×4.45 arcmin) of the images using the SExtractor analysis package (Bertin & Arnouts 1996).

Before running the search algorithm we first smoothed the final frames by convolving with a 2.5 px FWHM (~ 0.73 arcsec) Gaussian PSF, picking up those objects exceeding a $1\sigma_{bkg}$ threshold over the background RMS. This threshold corresponds to $2.2\sigma_{bkg}/\sqrt{N}$, N being the minimum detection area in pixels i.e the number of connected pixels within one seeing disk.

This rather low detection threshold provided a raw catalog from which we extracted different samples by varying the S/N limit in order to optimize completeness and minimize the number of spurious detections for a given magnitude limit. For example, at a $S/N = 5$ detection limit, compact objects as faint as $Ks = 23.0$ and $J = 24.8$ were detected in our images, compared with $Ks = 23.9$–24.5 and $J = 24.9$–25.2 as in the deepest Keck observations (Bershady et al. 1998; Djorgovski et al. 1995). We are therefore confident that our sample is not biased against the detection of small compact sources and that it is fully comparable with the deepest data previously obtained by other authors over smaller areas on the sky (Gardner et al. 1993; Soifer et al. 1994; McLeod et al. 1995; Djorgovski et al. 1995; Moustakas et al. 1997; Minezaki et al. 1998; McCracken et al. 1999). On the other hand, the isophotal photometry at the adopted surface brightness limit as reported in Table 1 directly affects the detection of extended sources and low surface brightness objects and is fully comparable with the data of Bershady et al. (1998) in their Keck images (i.e. K=23.9–24.2 mag/arcsec^2) or even deeper (J=25–25.5 mag/arcsec^2).

3.4. Magnitudes

Aperture photometry over a 2.5 arcsec circular diaphragm ($\sim 3\times$FWHM) has been derived for the whole sample and then offset by 0.25 mag both in J and Ks in order to account for their "total" flux according to the mean growth curve as for the brightest objects (Ks< 18.5, J< 20). In Fig. 1 the corrected aperture photometry is compared with the AUTO (Kron-like) magnitudes (Kron 1980) and isophotal magnitudes as calculated by SExtractor for the Ks-band selected sample.

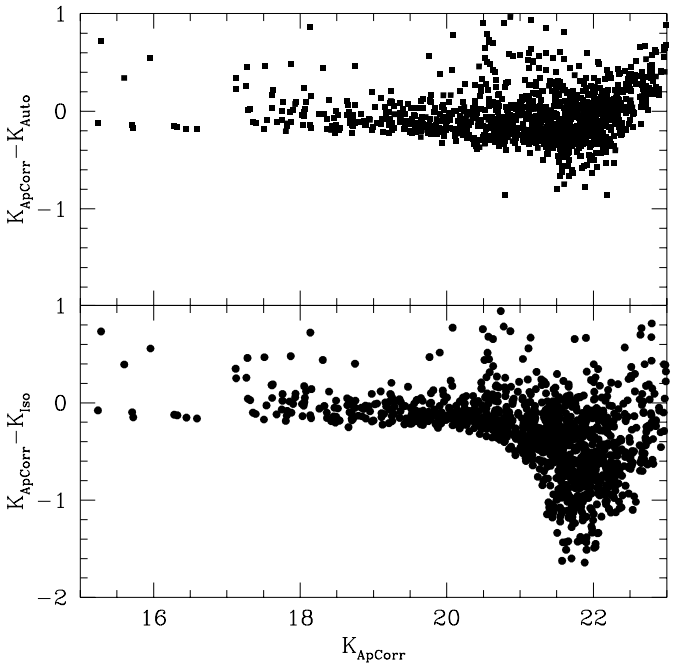

Fig. 1. Differences between the magnitude estimates for the Ks selected sample: (upper panel) difference between aperture corrected magnitude (K_{ApCorr}) and AUTO (Kron-like) magnitude (K_{Auto}); (lower panel) difference between aperture corrected magnitude and isophotal magnitude (K_Iso). The aperture correction (0.25 mag) between $2.5''$ and $5''$ has been obtained using a sample of sources brighter than Ks$= 18.5$.

A significant deviation is found between the three sets of magnitudes. Isophotal photometry tends to systematically underestimate the flux of faint objects, an effect which is significant also at bright magnitudes (Ks~ 20.5). To a lesser extent, an underestimate is also present in the case of the AUTO magnitude, especially in the two faintest magnitude bins (Ks> 21.5) where the background fluctuations become comparable to the signal even at a few pixels from the center of the sources.

3.5. Sample selection

On the basis of the adopted detection parameters (cf. Sect. 4.1), 1271 and 1743 sources have been recognized by SExtractor in the Ks and J images, respectively.

A measure of the detection reliability is now necessary in order to evaluate the number of spurious sources included in the sample, and their magnitude distribution. Since the completeness level in the detection algorithm is a function of object magnitude and size, our test will provide a guess of the optimum S/N ratio to eventually extract the fiducial J and Ks samples.

Operationally, we created a homogeneous set of noise images both in the J and Ks bands by combining unregistered frames. This assures a similar background as in the original data. The noise frames have then been "reversed" (i.e. multiplied by -1) in order to reveal the negative fluctuations and to

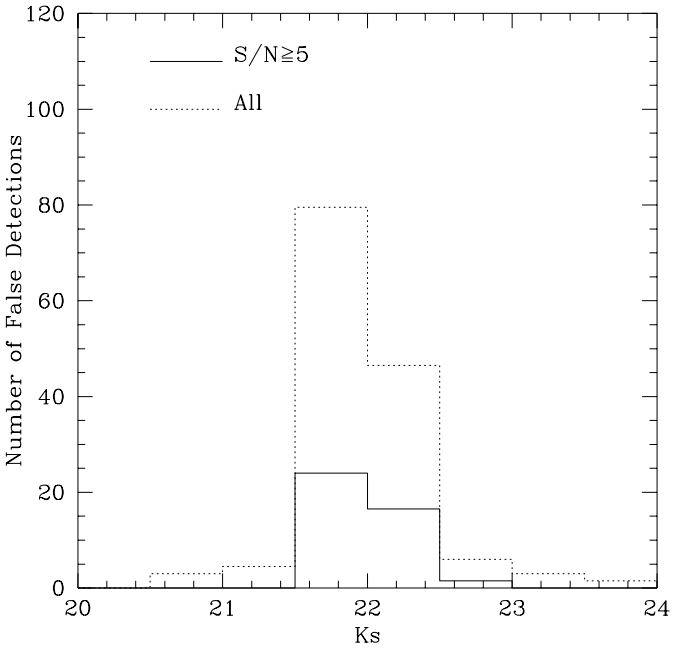

Fig. 2. Distribution of spurious sources. The dotted histogram refers to the distribution of detections with minimum S/N$=2.2$ within the seeing disk. The thick line describe the distribution of detections having S/N≥ 5.

make negative (i.e. undetectable) possible residuals of real objects. By running SExtractor with the same detection parameter set used to search for sources in the science frames, we have obtained the number of false detections which affect our data. The J band image is characterized by a very low noise and most of the spurious detections occur at a S/N$<$2.5 level. The Ks band image displays on the contrary a larger noise which consequently increases both the number of false detections as well as their S/N. In Fig. 2 we show the false detection distribution as a function of the Ks magnitude. From the figure, one sees that spurious detections would significantly affect photometry at low S/N, and a cutoff about S/N$\sim$5 seems to ensure the optimum threshold for confident object detection both in J and Ks within a 0.3 mag accuracy. In particular, using this cutoff the J selected sample is completely free from spurious detections and the K-selected one down to K=21.5, while they become $\sim 10\%$ at $21.5< Ks \leq 22.5$. On the basis of the above selection criterium our subsequent analysis will rely on the *bona fide* Ks and J samples containing 1025 sources down to Ks$\leq$22.5 and 1569 sources down to J$\leq$24.0. These samples are used throughout the rest of this paper.

4. Number counts and colors

4.1. Differential galaxy counts

In order to derive differential galaxy counts, we have first "cleaned" the two samples of stars. This has been done relying on the SExtractor morphological classifier. Stars were defined as those sources either brighter than Ks$=19$ or J$=20$, having a value of the "stellarity" index larger than 0.9 in both photometric bands.

Within the quoted magnitude limits, we verified that the J and Ks SExtractor classification coincides at a 95$\%$ confidence level while some discrepancy arises at fainter magnitudes where, however, the star contamination is negligible. It is worth noting that the adopted procedure tends to slightly overestimate the resulting galaxy counts both at faint magnitudes, where no count correction was applied, and at bright magnitudes where some fuzzy stars in the field could escape the cleaning procedure. On the other hand, our choice ensures that the galaxy samples are not biased against compact galaxies and that stellar samples are not contaminated by unresolved galaxies.

The second step in deriving galaxy counts concerns the completeness correction to our sample for faint, undetected galaxies. Obviously, this correction is larger at faint magnitudes and, in general, mainly depends on the source spatial structure. Such dependence is usually taken into account in the literature by introducing simulated sources with different typical profiles and magnitudes embedded in a Gaussian noise (e.g. Minezaki et al. 1998; Metcalfe et al. 1995) or in real frames (e.g. Saracco et al. 1997). These two methods suffer from the approximations introduced by the use of the "typical" profiles which cannot fairly reproduce the manifold of galaxy shapes.

A better approach would be to add to a real frame a grid of test sources artificially dimmed (e.g. Arnouts et al. 1999; Bershady et al. 1998; Yan et al. 1998). Template sources could be singled out from the brightest sources in the sample but a problem is that they might not conveniently span the whole range of size and shape of the faint galaxies. As a possible way out, we chose to generate a set of frames by directly dimming the final J and Ks frames themselves by various factors while keeping constant the background noise. The advantage of this procedure is of course to provide a fair artificial sample in the real background noise. SExtractor was then run with the same detection parameters to search for sources in each dimmed frame.

The correction factor c is the number of dimmed galaxies which should enter the fainter magnitude bin over the number of detected ones. Since we have selected the two samples at a S/N≥ 5 level, the correction factors refers to the number of such detections. By relaxing the selection criterion, using for example S/N=3, the factor c would decrease and it would be ~ 2 (i.e. a 50$\%$ completeness) in the faintest magnitude bin.

The raw counts n_r, the completeness correction factors c, the counts per square degree corrected for incompleteness N and their errors σ_N are reported in Table 2. The number uncertainty σ_N has been derived by quadratically summing up the Poissonian error $\sigma_{n_r} = \sqrt{n_r}$ of raw counts, the uncertainty in the completeness factor $\sigma_c = (N/n_r)\sigma_{n_r}$ and the contribution σ_ω due to clustering fluctuations. For an angular correlation function with a power law form $\omega(\theta) = A_\omega \theta^{-(\gamma-1)}$ ($\gamma = -1.8$) and a circular window function of radius θ_0, the expected fluctuations are

$$\sigma_\omega \sim \omega(\theta)^{1/2} \bar{N} \qquad (1)$$

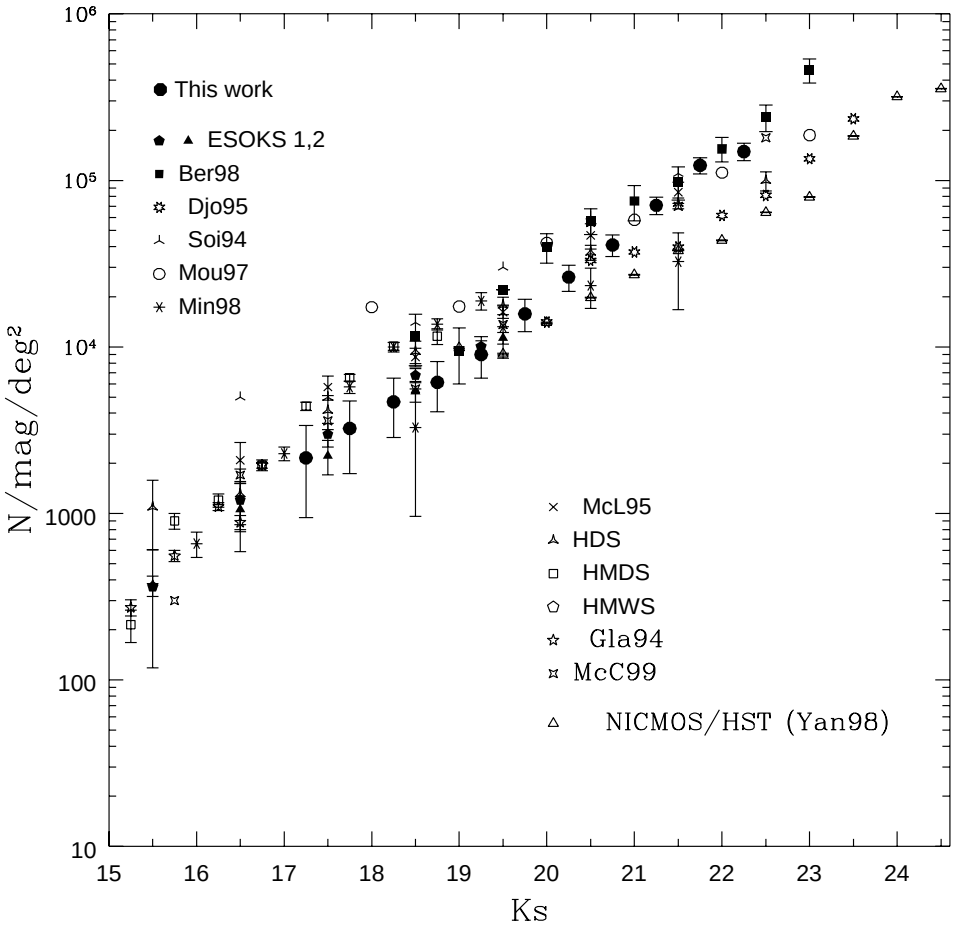

Fig. 3. The figure compares the Ks-band counts obtained in this work with those in the literature: Djorgovski et al. (1995, Djo95), Bershady et al. (1998, Ber98) (obtained at the Keck telescope), Gardner et al. (1993, HMWS, HMDS, HDS), Glazebrook et al. (1994, Gla94), Soifer et al. (1994, Soi94), McLeod et al. (1995, McL95), Moustakas et al. (1997, Mou97), Saracco et al. (1997, ESOKS1, 2), Minezaki et al. (1998, Min98) and McCracken et al. (1999, McC99). NICMOS/HST H-band counts of Yan et al. (1998, Yan98) are also shown. The slope of our counts ($\sim$0.38) agree very well with those obtained by McL95, Djo95 and Ber98 while it is significantly steeper than the slope obtained by Gardner et al. (1993) and by Mou97.

We have assumed that the amplitude A_ω evolves with magnitude following the relation $\log A_\omega \sim -0.3\times$mag (Brainerd et al. 1994; Roche et al. 1996) and that $\theta_0 \sim 150''$, which is the radius of a circle having an area corresponding to our fields. In Table 2 the derived amplitude A_ω is also reported for each magnitude bin. The values of the amplitudes are consistent with the results in the literature based on infrared selected samples (Roche et al. 1998; Carlberg et al. 1997. It is worth noting that while at bright magnitudes (Ks<19 and J<20) the poissonian error is comparable to the uncertainties introduced by clustering fluctuations ($\sigma_{n_r} \sim \sigma_\omega$) at magnitudes Ks$\sim$22 and J$\sim$23 $\sigma_\omega = 2 \times \sigma_{n_r}$ and, in the faintest magnitude bins, the single contributions to the total uncertainty σ_N are among them as $\sigma_{n_r} : \sigma_c : \sigma_\omega = 1 : 3.8 : 2.7$.

The total number of sources in Table 2 are 874 for the Ks-band and 1285 for the J-band and represent the largest samples currently available at these depths.

Fig. 3 shows the Ks-band galaxy counts derived here compared with those in the literature[1]. Our counts follow a $d logN/dK$ relation with a slope of 0.38 in the magnitude range $17 < K < 22.5$ and do not show evidence of any turnover or flattening down to the limits of the survey.

[1] A recent paper by Ferreras et al. (1998) presents galaxy counts down to K=19 but they do not provide sufficient data to derive (and thus reproduce here) their counts.

In Fig. 4 our J-band galaxy counts are compared with those of Bershady et al. (1998) which are the only J-band data available in the literature. For the J number counts we obtain a slope $\sim$0.36 in the magnitude interval $18 < J < 24$. As for the Ks trend, J counts do not show any sign of flattening down to the limits of the data.

4.2. Galaxy colors

The 2.5 arcsec aperture J-K color of galaxies in our sample was obtained by running SExtractor in the so-called *double-image mode*: J magnitudes for the Ks selected sample have been derived using the Ks frame as reference image for detection and the J image for measurements only and *vice versa* for the J selected sample. This method forces the program to carry out a net flux measurement within the aperture centered on the position of the source detected in the reference frame.

In order to avoid unreliable measurements, that is net flux simply due to local background fluctuations, we have considered as genuine estimates those signals exceeding 1.5σ above the background within the 2.5 arcsec diameter aperture (Ks$_{lim} = 23.05$, J$_{lim} = 24.8$). Fainter signals have been considered unreliable and they have been replaced by a 1.5σ upper limit. In Table 3 the number of galaxies, the median J-Ks color, the standard deviation and the number of lower and upper limits to J-Ks

Table 2. Differential number counts in the Ks-band (upper panel) and in the J-band (lower panel) derived from the samples including sources having S/N≥5. Errors σ_N take into account the Poissonian error on raw counts (n_r), the uncertainties in the incompleteness correction factor c and the fluctuations due to clustering (see text). The amplitude A_ω of the angular correlation function has been obtained using the scale relation $\log(A_\omega) \sim -0.3$mag+cost.

Ks	n_r	c	$N/mag/deg^2$	σ_N	$A_\omega(\theta'')$
15–17	4	1.0	360	***	***
17.25	6	1.0	2160	1215	8.2993
17.75	9	1.0	3240	1510	5.8755
18.25	13	1.0	4680	1825	4.1595
18.75	17	1.0	6120	2048	2.9447
19.25	25	1.0	9000	2508	2.0847
19.75	44	1.0	15840	3520	1.4758
20.25	73	1.0	26280	4743	1.0448
20.75	114	1.0	41040	6106	0.7397
21.25	197	1.0	70920	8550	0.5237
21.75	263	1.3	123100	13898	0.3707
22.25	109	3.7	145200	17987	0.2624
J	n_r	c	$N/mag/deg^2$	σ_N	$A_\omega(\theta'')$
16–18	4	1.0	360	***	***
18–19	12	1.0	2160	1215	8.2993
19.25	10	1.0	3600	1634	5.8755
19.75	15	1.0	5400	2033	4.1595
20.25	18	1.0	6480	2137	2.9447
20.75	33	1.0	11880	3097	2.0847
21.25	64	1.0	23040	4738	1.4758
21.75	82	1.0	29520	5203	1.0448
22.25	153	1.0	55080	7770	0.7397
22.75	253	1.0	91080	10548	0.5237
23.25	417	1.2	180144	21349	0.3707
23.75	224	2.8	225800	23828	0.2624

in each magnitude bin are reported for the Ks and J sample, respectively.

In Figs. 5 and 6 color-magnitude diagrams of the whole Ks and J galaxy samples are shown together with the median locus. The error bars are the standard deviation from the mean of the values within each bin.

The most notable feature in both figures is a break in the color trend. The intervening redder J-Ks with increasing magnitude, as induced by the k-correction, turns in facts to bluer values for the galaxies fainter than $Ks \sim 19$ or $J \sim 20$. We will discuss this important issue in Sect. 6.

5. Galaxy size and number counts

5.1. Compactness index

A reasonable measure of the apparent size of distant galaxies, represents a critical step in the analysis of faint galaxy samples (Petrosian 1998) and hence in the application of cosmological tests. Given the cosmological dimming of the apparent surface brightness (SB), galaxy isophotal radius would be a poor measure of apparent size, especially for the faintest objects in a deep survey. A fixed isophotal threshold would not necessarily span a similar absolute size of galaxies at different redshifts. Special care has therefore to be taken in estimating the galaxy metric size in a way which is independent on the redshift and source profile and takes into account the photometric bias (Djorgovski & Spinrad 1981; Kron 1995; Petrosian 1998).

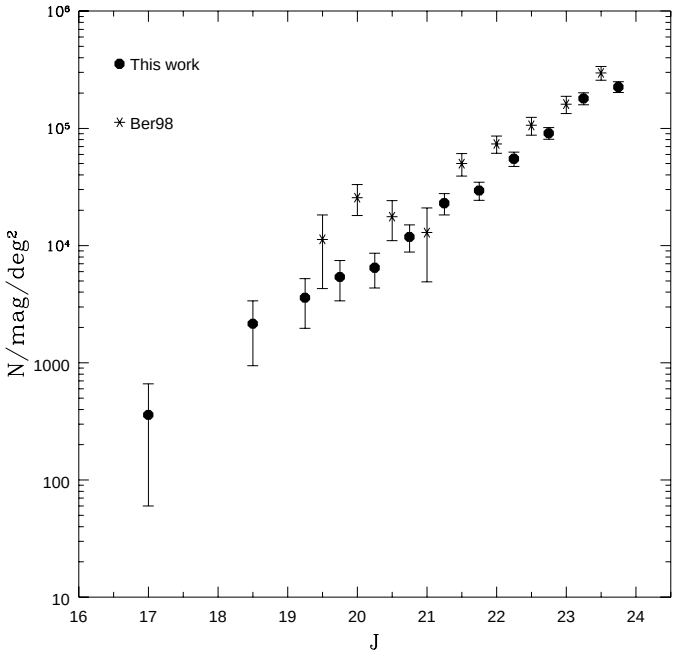

Fig. 4. The J-band galaxy counts obtained in this work are compared with those previously obtained by Bershady et al. (1998, Ber98). The J-band counts continue to rise with a power law slope of ∼0.36 showing no signs of flattening down to $J = 24.0$.

For our samples, we adopted the metric size function $\eta(\theta)$ first introduced by Petrosian (1976) defined as

$$\eta(\theta) = \frac{1\ d\ ln\ l(\theta)}{2\ d\ ln(\theta)} \tag{2}$$

(Kron 1995) where $l(\theta)$ is the growth curve. This function has the property

$$\eta(\theta) = \frac{I(\theta)}{\langle I \rangle_\theta} \tag{3}$$

where $I(\theta)$ is the surface brightness at radius θ and $\langle I \rangle_\theta$ is the mean surface brightness within θ.

The function $\eta(\theta)$ has been obtained for each galaxy by constructing its own intensity profile. The intensity profiles have been derived from the J and Ks frames through equi-spaced (0.146 arcsec) multi-aperture photometry after a 2×2 re-sampling of the images. Following Bershady et al. (1998), we define the galaxy angular size the value of θ_η such that $\eta(\theta_\eta) = 0.5$ as obtained by a spline fit interpolation across each object. The median $\theta_{0.5}$ values are 0.73 arcsec and 0.79 arcsec for the J and Ks samples, respectively. For reference, the measured angular size of point sources in our images is $\theta_{0.5} = 0.67$ arcsec. In order to simplify comparison of these

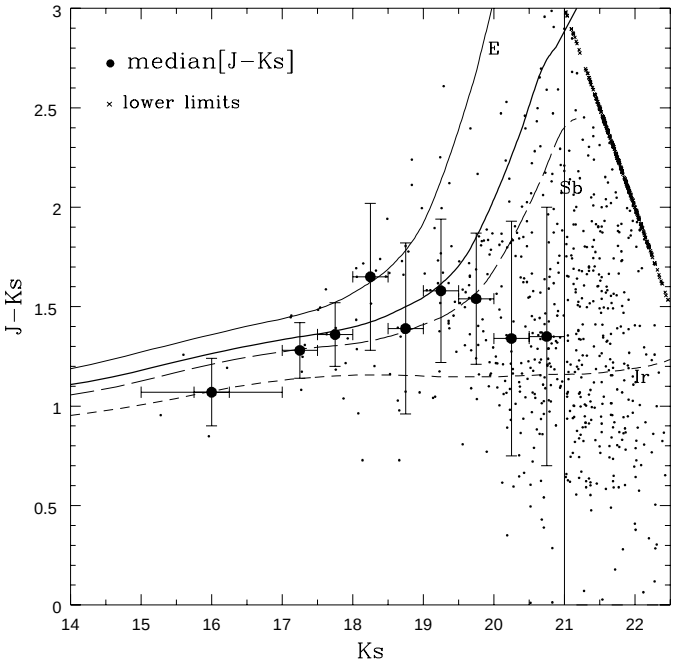

Fig. 5. Color-magnitude diagram of our Ks galaxy sample. Large filled points represent the median J-Ks color. Vertical error bars are the standard deviation from the mean. The bin widths (usually 0.5 mag) are represented by the horizontal bars. Small crosses mark undetected J galaxies, i.e. the J-Ks lower limits. The vertical straight line represents the completeness J-band detection limit for the Ks sample. The thick solid curve is the expected apparent color of a local galaxy mix (see Sect. 6.2 and Table 4) evolved back to high redshift ($z > 10$) according to the models of Buzzoni (1998). The expected J-K color for a pure galaxy population of E (thin solid line), Sb (long-dashed line) and Im (short-dashed line) types is also reported as labeled in the figure. Models assume a ($H_o, q_o = 50, 0.5$) cosmology.

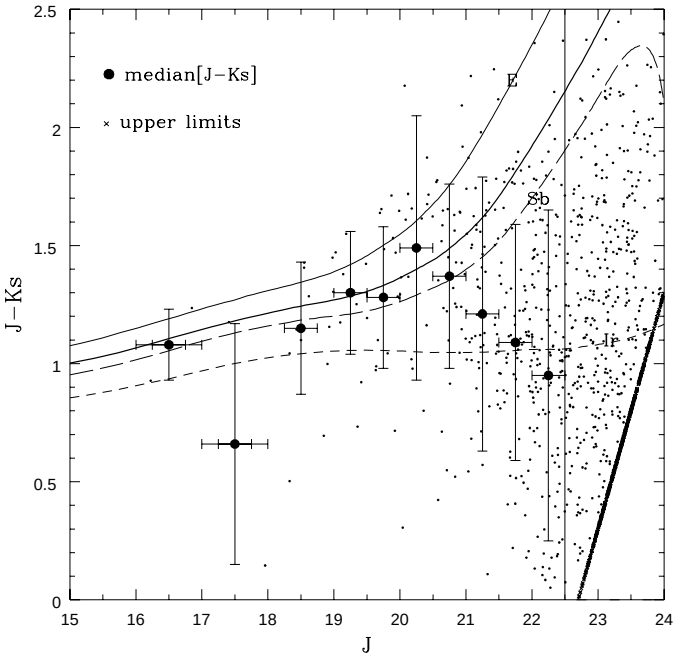

Fig. 6. Same as Fig. 5 but for the J-selected galaxies. The vertical solid line indicates the detection limit of the J sample in the Ks frame.

angular sizes with those in the literature we have also measured for each galaxy the effective radius θ_{eff}. The result is that $\theta_{eff} \simeq 0.6 \cdot \theta_{0.5}$ for our samples, which agrees with the effective radius measured by Yan et al. (1998).

According to the fiducial galaxy size, we were also able to derive a compactness parameter via the luminosity concentration index C_η

$$C_\eta = \frac{F(< \theta_{0.5})}{F(< 1.5\theta_{0.5})} \tag{4}$$

that is the ratio between the flux within the radius $\theta_{0.5}$ and that within $1.5\theta_{0.5}$. This dimensionless parameter varies in the range $0 < C_\eta < 1$ increasing in the most compact objects and vanishing in amorphous galaxies. The estimated values of C_η for simulated spiral and elliptical profiles (convolved with the observed PSF) are 0.69 and 0.74 respectively, to be compared with $C_\eta = 0.9$ of the PSF. Note that, by definition, C_η is free of any adopted surface brightness threshold in the photometry, and is therefore *not* affected by galaxy redshift as for instance the central concentration index C defined by Abraham et al. (1994; 1996) and discussed by Brinchmann et al. (1998). The concentration index C_η and the apparent radius $\theta_{0.5}$ for the whole Ks and J samples are given in Figs. 7 and 8, respectively, together with their median locus. In the figures, error bars are the standard deviation from the mean within each bin. The median values $med[\theta_{0.5}]$ and $med[C_\eta]$ and the relative standard deviations are listed in Table 3.

The compactness index seems to be constant down to Ks$\sim$ 19 and J$\sim$ 20 whereas going to fainter magnitudes it is evident that the galaxies become systematically more compact. This trend is clearly present in both the samples as shown by the increase of the median values of C_η with increasing apparent magnitude. It is worth noting that the increasing compactness of galaxies occurs in the same magnitude range where galaxies also become bluer. Moreover, this trend seems to be matched also by a decrease of the apparent size of galaxies, a trend which is more evident in the Ks sample (Fig. 7) and which was found also by Yan et al. (1998). However both apparent size and color depend on redshift and while the former change less than 20% beyond $z = 0.7$ the latter continues to change substantially. We would like to stress that, while the apparent size is a redshift dependent parameter and hence its systematic decrease to fainter magnitudes could be attributed to a systematic increase of redshift, *the compactness index defined by (4) is redshift independent and its trend with apparent magnitude thus represents a real physical behavior of faint galaxies*.

5.2. Number counts vs size

Following Bershady et al. (1998), we divided the J and Ks galaxy population in two sub-samples of small (s) and large (l) objects relative to the median $\theta_{0.5}$ value (i.e. med[$\theta^J_{0.5}$]=0.73 arcsec, med[$\theta^{Ks}_{0.5}$]=0.79 arcsec).

A suitable completeness estimate is a critical step in this case. For a given total magnitude the mean surface brightness of a source depends on its size so that larger galaxies tend to be less

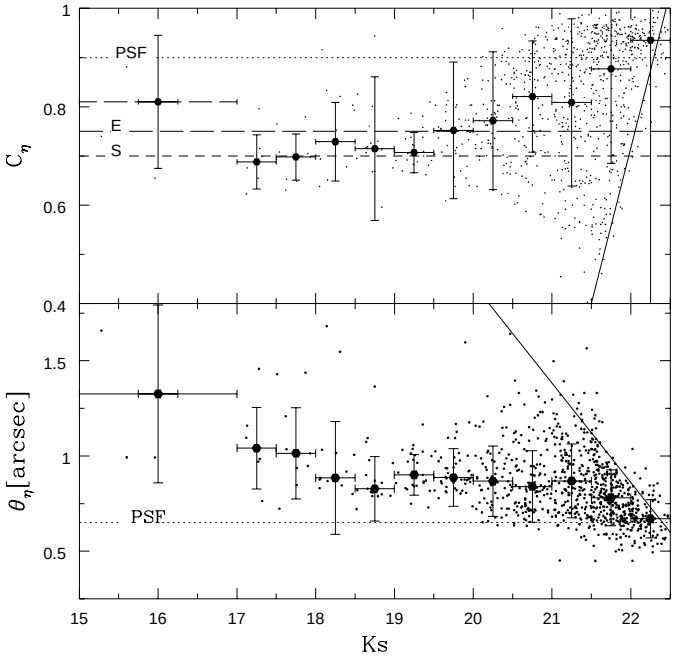

Fig. 7. Compactness index C_η (upper panel) and apparent size $\theta_{0.5}$ (lower panel) as a function of Ks magnitude. The filled (red) circles are the median values in a 0.5 mag bin width. Vertical error bars are the standard deviation in each magnitude bin while horizontal bars represent the bin width. The dotted, the dashed and the long-dashed lines in the upper panel indicate the values of C_η for PSF, Spiral and Elliptical profiles respectively (see Sect. 5.2). The solid line in the lower panel shows the magnitude enclosed in an aperture of radius θ and a uniform surface brightness Ks=22.76 mag/arcsec^2 while the dotted line represent the characteristic size of a point source in our images.

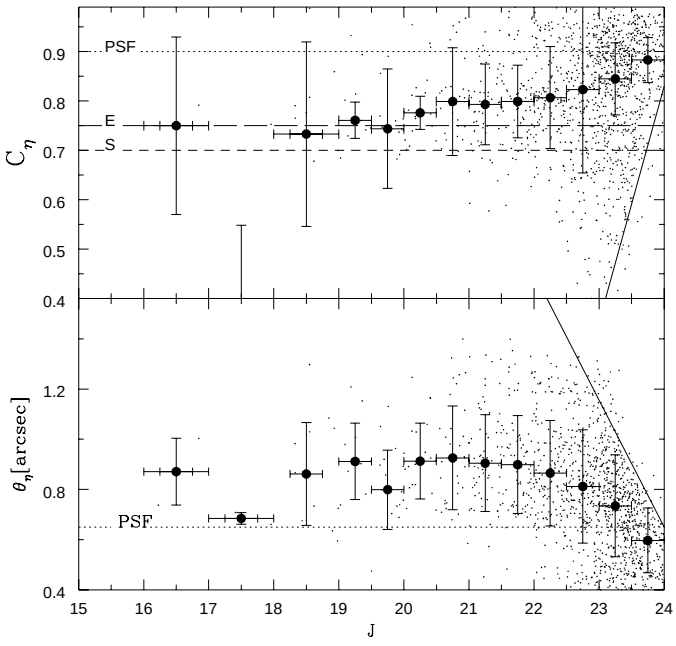

Fig. 8. Same as in Fig. 7 but for the J sample. The solid line in the lower panel shows the magnitude enclosed in an aperture of radius θ and a uniform surface brightness of J=23.88 mag/arcsec^2.

Table 3. Median (J-Ks) color, size and compactness index of the galaxy sample. Errors are the standard deviation in each bin. The number of lower and upper limits (L.L., U.L.) represents, in the upper panel, the number of galaxies in each magnitude bin belonging to the Ks sample undetected in the J frame and, in the lower panel, the J-band selected galaxies undetected in the Ks image. Lower and upper limits to the J-K color are marked with $^\uparrow$ and $^\downarrow$ respectively.

Ks	Gal	med[J-K]	σ	L.L.	med[$\theta_{0.5}$]	σ	med[C_η]	σ
16.00	4	1.07	0.2	0	1.33	0.5	0.81	0.1
17.25	6	1.28	0.1	0	1.04	0.2	0.69	0.1
17.75	9	1.36	0.2	0	1.01	0.2	0.70	0.05
18.25	13	1.65	0.4	0	0.88	0.3	0.73	0.1
18.75	17	1.39	0.4	0	0.83	0.2	0.71	0.1
19.25	25	1.58	0.4	0	0.90	0.1	0.71	0.04
19.75	44	1.54	0.3	0	0.89	0.1	0.75	0.1
20.25	73	1.34	0.6	1	0.87	0.2	0.77	0.1
20.75	114	1.35	0.7	0	0.84	0.2	0.82	0.1
21.25	197	$1.65^\downarrow$	0.8	24	0.87	0.2	0.81	0.2
21.75	263	$2.16^\downarrow$	0.7	109	0.78	0.1	0.88	0.2
22.25	109	$1.84^\downarrow$	0.7	50	0.67	0.1	0.93	0.7
J	Gal	med[J-K]	σ	U.L.	med[$\theta_{0.5}$]	σ	med[C_η]	σ
16.50	2	1.08	0.1	0	0.87	0.1	0.40	0.4
17.50	2	0.66	0.5	0	0.68	0.02	0.38	0.4
18.50	12	1.15	0.3	0	0.86	0.2	0.73	0.4
19.25	10	1.28	0.3	0	0.95	0.2	0.78	0.1
19.75	15	1.28	0.3	0	0.80	0.2	0.74	0.3
20.25	18	1.49	0.6	0	0.91	0.1	0.78	0.07
20.75	33	1.37	0.4	0	0.93	0.2	0.80	0.2
21.25	64	1.21	0.6	1	0.90	0.2	0.79	0.2
21.75	82	1.09	0.5	0	0.90	0.2	0.80	0.2
22.25	153	$0.95^\uparrow$	0.6	13	0.86	0.2	0.81	1.1
22.75	253	$0.63^\uparrow$	0.6	85	0.81	0.2	0.82	0.4
23.25	417	$0.86^\uparrow$	0.4	239	0.73	0.2	0.84	0.2
23.75	224	$1.22^\uparrow$	0.3	150	0.60	0.1	0.88	0.1

visible than smaller ones. Fortunately, the simulation procedure we devised in Sect. 5.1 allowed us to completely control this selection effect and derive a suitable completeness correction.

The differential galaxy counts for the s and l galaxies are shown in Fig. 9 which clearly reveals the different behavior followed by the s compared to the l sources: small sources show a lower surface number density at bright magnitudes, and a much steeper counts slope over the whole magnitude range. The slopes we derived for the s samples are essentially *Euclidean*. In particular we obtained $\gamma^s_{Ks} \sim 0.6$ and $\gamma^s_J \sim 0.56$ to be compared with $\gamma^l_{Ks} \sim 0.36$ and $\gamma^l_J \sim 0.38$ for the l sample. Supporting Bershady's et al. (1998) conclusions therefore, small sources dominate the number counts at faint magnitudes (Ks$>$21.5, J$>$ 23) where their number density is more than twice the number density of large sources.

In Figs. 10 and 11 the J-Ks color distributions of s and l galaxies are shown for the Ks and J sample respectively. The shaded histograms in each figure represent the distribution of the J-Ks lower limits (for the Ks selected sample) and upper limits (for the J selected sample).

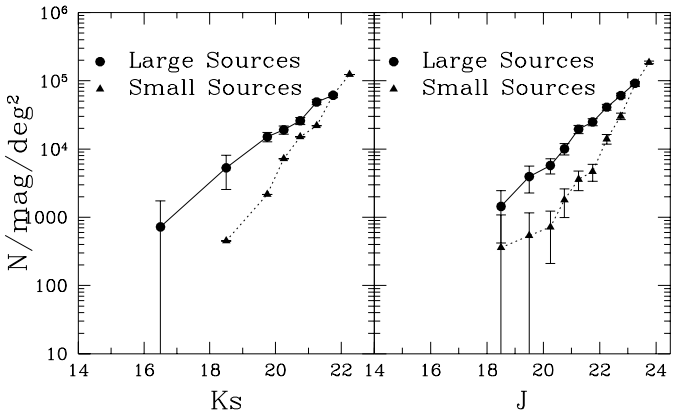

Fig. 9. Ks-band (left) and J-band (right) differential number counts for small and large galaxies: small galaxies are those having $\theta^K_{0.5} \leq 0.79$ arcsec and $\theta^J_{0.5} \leq 0.73$ arcsec. The slope of the counts are $\gamma^s_{Ks} \sim 0.6$ and $\gamma^s_J \sim 0.56$ for small sources and $\gamma^l_{Ks} \sim 0.36$ and $\gamma^l_J \sim 0.38$ for large sources.

Table 4. Observed median (J-Ks) color as a function of apparent magnitude for *s* and *l* sources in the Ks and J samples. Lower and upper limits to the J-K color are marked with $^\uparrow$ and $^\downarrow$ respectively.

Class	17.5	18.5	19.5	20.5	21.5	22.5	23.5
s_K	1.40	1.62	1.52	1.17	$1.82^\downarrow$	$1.48^\downarrow$	—
l_K	1.34	1.48	1.54	1.45	$2.01^\downarrow$	$1.83^\downarrow$	—
s_J	—	0.66	0.69	0.72	0.70	$0.67^\uparrow$	$0.57^\uparrow$
l_J	—	1.13	1.34	1.40	1.12	$1.02^\uparrow$	$0.78^\uparrow$

Large sources tend to have a sharper distribution and a redder median J-Ks color compared to s sources. Moreover, the latter are skewed toward bluer colors. Such differences between the J-Ks color distributions of s and l sources are highly significant for both samples. The two distributions have been first compared by performing a K-S test on the complete color samples, that is samples limited to Ks$\leq$ 21 and J$\leq$ 22, in order to avoid uncertainties introduced by the presence of censored data. In addition, we have extended the comparison to the whole sample by making use of "survival analysis" (Avni et al. 1980; Isobe et al. 1986; Feigelson & Nelson 1985). In particular we have compared the two sample distributions with the generalized Wilcoxon test, which is able to treat data including lower and upper limits equally and obtaining a high significance (10^{-3}).

In Table 4 we report the median J-Ks in 1 mag bin width for s and l sources of the Ks and J sample while Fig. 12 shows the color-magnitude diagrams of s and l sources. It can be seen the higher fraction of blue galaxies in the sample of s sources at faint magnitudes with respect to l sources as confirmed by the values reported in Table 4.

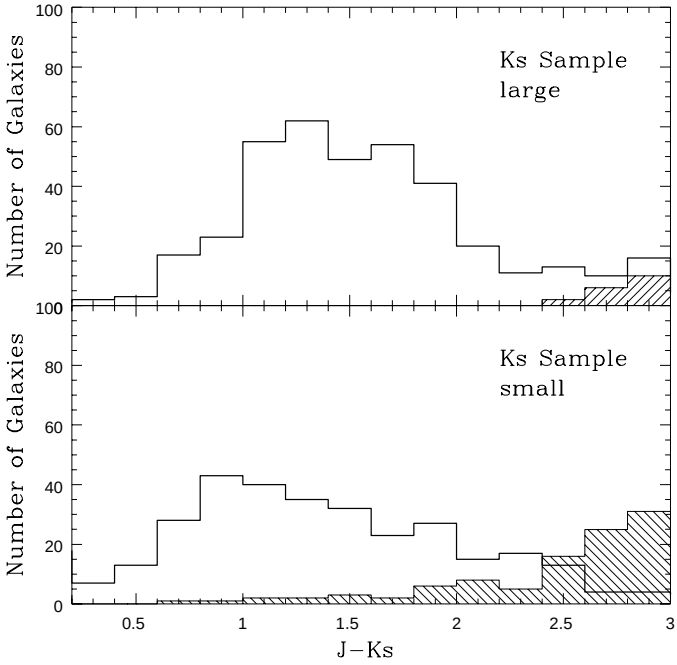

Fig. 10. J-Ks color distributions (thik histograms) for l (upper panel) and s sources (lower panel) belonging to the Ks sample. The shaded histograms represent the distribution of the J-Ks lower limits i.e. galaxies redder than $J_{lim} - Ks$ (J$_{lim} = 24.8$, Sect. 4.2).

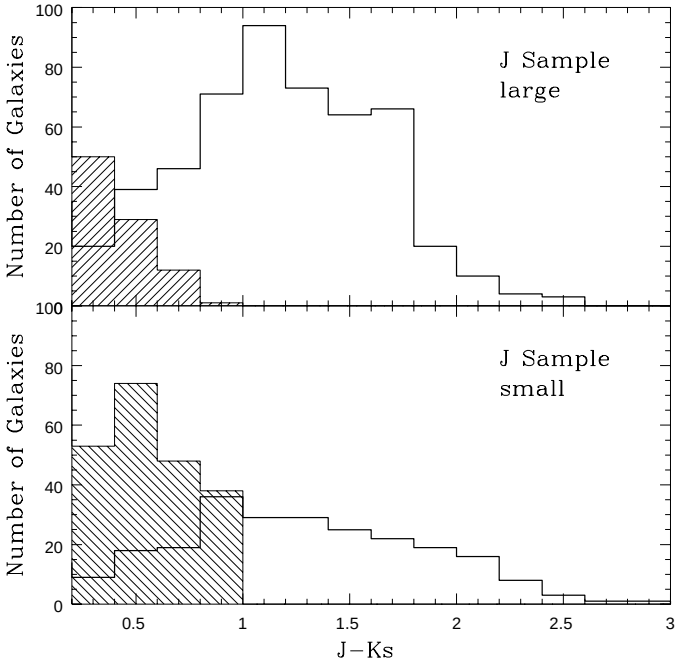

Fig. 11. J-Ks color distribution for l (upper panel) and s sources (lower panel) belonging to the J sample. The shaded histograms represent the distribution of the J-Ks upper limits i.e. galaxies bluer than $J - Ks_{lim}$ (Ks$_{lim} = 23.05$, Sect. 4.2).

6. Discussion

6.1. Galaxy counts

In Fig. 3 we have compared our Ks-band galaxy counts with those derived by other authors. The remarkable scatter between the different surveys is probably due to a combination of various factors: slightly different filters (K, K', Ks), differences in the treatment of star contamination and in the magnitude estimate (aperture or isophotal or pseudo-total), large scale fluctuations,

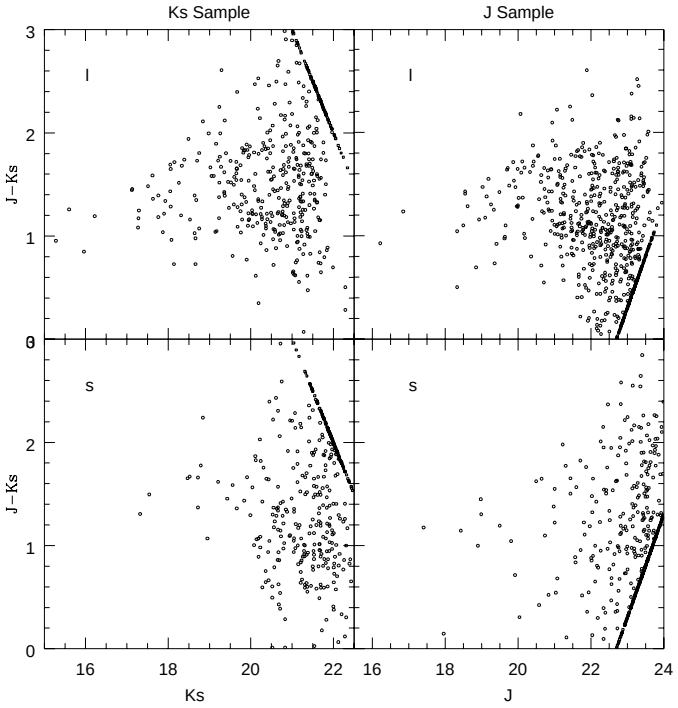

Fig. 12. Color-magnitude diagram of *s* (lower panel) and *l* (upper panel) sources for Ks sample (left) and J sample (right).

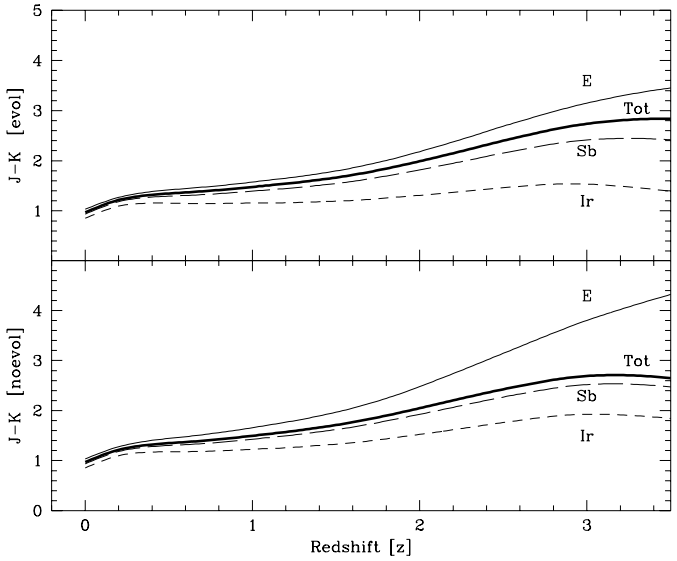

Fig. 13. Expected J-Ks color of different galaxy types as a function of redshift in the case of no-evolution (lower panel) and evolution (upper panel). The mean expected color of the local galaxy mix as in Marzke et al. (1998) is also shown (thick solid line).

field selection criteria and, finally, possible systematics in the photometric calibrations. The largest deviation occurs between the Soifer et al. (1994) counts, defining the highest surface density at magnitudes K>19, and those of Djorgovski et al. (1995) and Minezaki et al. (1998) which define the lowest surface density of objects in this magnitude range. The amplitude of our counts at magnitude brighter than Ks=20 agrees with that derived by Glazebrook et al. (1994), Saracco et al. (1997) and with that obtained by Minezaki et al. (1998) in the bright survey, while it is significantly lower than the amplitude of HMDS and HDS (Gardner et al. 1993) and of McLeod et al. (1995). At fainter magnitudes (Ks≥ 20) we obtain a surface density of objects consistent with that of Bershady et al. (1998) and McLeod et al. (1995) but significantly higher than that of HDS (Gardner et al. 1993; Cowie et al. 1994) and Djorgovski et al. (1995). It is worth noting that the area covered by these surveys, and consequently the number of sources, is at most one fifth of that surveyed in this work. This obviously amplifies the scattering due to large-scale fluctuations. However, rather than the amplitude, the most striking feature of the plot is the slope of the number counts. Contrary to Gardner et al. (1993) and Moustakas et al. (1997) who obtain a slope in the range 0.23–0.26 for $18 < K < 22$, we obtain a significantly steeper slope of 0.38. This result confirms the previous work by McLeod et al. (1995), Soifer et al. (1994) and Saracco et al. (1997) at K<21 and Djorgovski et al. (1995), Bershady et al. (1998) and McCracken et al. (1999) down to K=23–24. Moreover, the slope of our K-band counts, and the lack of any flattening at its faint end, are both independently confirmed also by the J-band counts which indicate a slope of ~ 0.36 in agreement with the result of Bershady et al. The overall conclusion is therefore that *galaxy counts in the near IR continue to rise with no evidence of a turnover or a flattening down to the current magnitude limit of the observations.*

6.2. Colors and galaxy counts

Which galaxies are responsible for the continuous increase of IR counts at very faint magnitudes? The two main observational results indicate that *i)* at Ks>19 and J>20.5 the median J-Ks color of the galaxy population turns bluer, as shown in Figs. 5 and 6 and summarized in Table 3; *ii)* the same surface density of objects at Ks$\sim$22 is reached at J~ 23, which implies that the bulk of the population of galaxies at these apparent magnitudes should have a mean color J-Ks~ 1, in agreement with the observed J-Ks color trend.

In Fig. 13 the expected J-K color of galaxies for different morphological types and that expected for the local galaxy mix are shown as a function of redshift for evolving and non evolving galaxies. Model predictions are based on Buzzoni's (1989, 1995) population synthesis code. Three sets of model galaxies have been computed to ease comparison with the observations. The evolution of ellipticals (E) is accompanied with that of Sb spirals and Im irregulars. As in the standard scenario, ellipticals are assumed to be suitably described by a single burst stellar population while irregulars follow a flat star formation rate at every age. The intermediate case of Sb spirals, on the contrary, takes into account a declining star formation rate in the disk ($SFR \propto t^{-0.5}$) coupled with a spheroidal component (bulge+halo) as in the ellipticals (see Buzzoni 1999 for more details on the model templates). From the figure, galaxies with J-Ks~ 1 are compatible with redshifts $z \sim 0.2$–0.3, and a value of J-K< 1.5 seems to be consistent with a reshift no larger

Table 5. Type-dependent LFs, optical-near-IR colors and morphological mix used in the models

Type	α	ϕ_* 10^{-4} Mpc^{-3}	M_B^*	B-J	J-K	M_J^*	M_K^*	f_B	f_J	f_K
E	-1.00	5.5	-20.88	3.19	1.03	-24.07	-25.10	29%	44%	46%
Sb	-1.11	10.0	-20.94	2.58	0.94	-23.52	-24.46	61%	51%	49%
Irr	-1.81	0.2	-21.29	2.10	0.85	-23.39	-24.24	10%	5%	5%

than $z \sim 1$ as shown by the model representing the mean color weighted by the local galaxy mix (Tot). However it should be mentioned that IR colors alone are not sufficient to strongly constraint redshifts.

One major advantage of the J and K_s infrared data is that we are probing the flatter and relatively shallower region of the rest-frame galaxy spectral energy distribution. The only significant flux discontinuity, coming from the Balmer break, only enters the J band well beyond $z \sim 2$. In any case, the net effect of redshift on the apparent infrared colors is a smooth reddening with increasing distance resulting in high-z galaxies somewhat resembling local M-type stars in the Galactic field. More generally, therefore, up to $z \sim 3$, a sequence in apparent $J-K$ color can also be regarded as a monotonic sequence in distance for galaxies of the same morphological type. In Figs. 5 and 6, the theoretical J-K colors for the three different morphological types are compared with those observed as a function of the apparent J and Ks magnitudes. In addition, we also show the expected colors for the local galaxy mix as a whole derived by taking into account the present-day luminosity function as in Marzke et al. (1998). Operationally, the B Schechter parameters for the different morphological types (cf. Table 1 in Marzke et al. 1998) have been combined with the theoretical $B-J$ and $B-K$ colors to obtain the mean J and K luminosity contribution from early, late and irregular galaxies. For each galaxy subsample (i), this is simply assumed to be proportional to $\int L_i \phi_i(L)$ where $\phi_i(L)$ is the appropriate Schechter function so that

$$\frac{L_i}{L_{TOT}} = \frac{\Gamma(2+\alpha_i)\ \phi_i^*\ L_i^*}{\sum \Gamma(2+\alpha_i)\ \phi_i^*\ L_i^*} \tag{5}$$

summing up over the running index i for ellipticals, spirals and irregulars. For each galaxy template and for the local galaxy mix we finally computed the apparent $J-K$ color as well as the apparent magnitude of a reference M^* galaxy in a $(H_0, q_0) = (50, 0.5)$ cosmology. The resulting luminosity partition in the different (rest-frame) photometric bands at $z \to 0$ is summarized in Table 5 (note of course that the Marzke et al. relevant values for M^* and ϕ^* have been rescaled in the table according to $H_0 = 50$ Km s^{-1} Mpc^{-1}).

Since model refers to L^* galaxies (that have *reference* but not necessarily *mean* luminosity for each morphological type), the natural expectation, when comparing with real galaxy samples, as in Figs. 5 and 6 for instance, is that models provide a sort of brighter (and somewhat redder) envelope to the data. This is because the real "baricenter" of the luminosity distribution at any z is always slightly fainter (and bluer) than L^*, depending on the faint-end tail of LFs.

Even if the model is consistent with the observed color of galaxies at bright magnitudes, it completely fails to match the observed trend at faint magnitudes where galaxies are much bluer than expected. The hypothesis of a high redshift galaxy population ($z > 1$) dominating the faint counts is thus unacceptable. Even in the case that Irregular galaxies would prevail the colors should be much redder than J-K~ 1. Apparently, the equivalence *fainter magnitudes* $\simeq$ *higher redshifts* is therefore not supported by the observations.

A similar relationship between color trend and redshift distribution of faint galaxies has also been found by Cowie et al. (1996). In their sample, they find that blue objects dominate the K counts and that a huge fraction of their K-selected faint objects are in fact extremely blue in (I-K). Moreover, the observed median redshift of faint galaxies appears to be lower than expected for L^* galaxies seen at the same apparent K magnitude, while galaxies display a roughly constant or even decreasing K luminosity with increasing redshift at least at K≤ 19 where the redshift completeness is high.

As the high-reshift solution ($z > 1$) seems to be inconsistent with the photometric properties of faint IR galaxies, we have to investigate the possibility of a local ($z < 0.3$) origin of these galaxies.

A galaxy seen at Ks$\sim$22 and placed at $z \sim 0.3$ would display an absolute magnitude not brighter than $M_K \sim -19$ (assuming H$_0$=50 Km s^{-1} Mpc^{-1}, q$_0$=0.5). Integrating the local IR luminosity function (LF) of galaxies in Gardner et al. (1997) described by $\alpha \sim -1$ and $M_K^* \sim -24.5$, within $z \sim 0.3$ and $M_K \geq -19$ we derive, in the magnitude range $21 < K < 22$, a surface density of galaxies 20–40 times lower than observed. A large uncertainty in such estimates derives from the different values of the normalization parameter ϕ^* of the LF obtained by various authors which can vary by more than a factor of two (see e.g. Efsthathiou et al. 1988; Lilly et al. 1995; Zucca et al. 1997; Mobasher et al. 1993; Glazebrook et al. 1995b; Gardner et al. 1997; Cowie et al. 1996). Using a high normalization (e.g. $\phi^* \simeq 0.005$ Mpc^{-3} as in Marzke et al. 1994) the observed surface density of galaxies can be obtained within $z \sim 0.3$ by assuming a slope of the faint end LF $\alpha \leq -1.8$.

Some indications of a flat ($\alpha \sim -1$) faint-end LF in the near IR come from the work of Gardner et al. (1997), Mobasher et al. (1993) and Glazebrook et al. (1995). However, it is worth noting that all of the previous work has sampled the LF at relatively bright IR luminosity ($M_K < -20$) and thus misses the crucial piece of information to assess our problem. On the contrary, some hints in favor of a steeper LF for field galaxies at infrared wavelengths come from Szokoly et al. (1998) who find a slope

$\alpha \sim -1.3$. The small sample of galaxies used in that work (one fourth of that used by Gardner et al.) cannot, however, place severe constraints on the value of α. Stronger evidences of a steep K-band LF of field galaxies come from Bershady et al. (1999) which obtain $\alpha \sim -1.6$.

Evidence for a steeper slope of the IR LF are also found for cluster galaxies ($\alpha \sim -1.4$, Mobasher & Trentham 1998; $\alpha \sim -2$, De Propris et al. 1998a) and, in the optical bands, both in the cluster environment (e.g. De Propris et al. 1998b; Lobo et al. 1997; Bernstein et al. 1995; Driver et al. 1994; Molinari et al. 1998) and in the field[2]: Marzke et al. (1994) find $\alpha \sim -1.8$ for the LF of very late type and irregulars galaxies (see also Marzke and Da Costa 1997; Marzke et al. 1998); Zucca et al. (1997) find a rising LF at magnitudes fainter than $M_{b_j} \sim -16$ which is well fitted by a power law with slope $\beta = -1.6$ and, finally, Liu et al. (1998) find $\alpha \sim -1.85$ for the U-band LF of galaxies bluer than Sbc.

Faced with the lack of reliable information on deep IR LFs in the field but with emerging evidence from optical investigations, we are inclined to believe that a genuine steepening of the LF at its faint-end tail cannot be ruled out and that a prevailing population of sub-L^*_K (and hence low mass and low redshift ($z < 1$)) galaxies may dominate at faint infrared magnitudes.

6.3. Sizes, compactness and galaxy counts

From Figs. 7 and 8 we can infer that the faint IR population mainly consists of galaxies which are intrinsically compact compared to those seen at brighter apparent magnitudes. Fig. 9 also shows that the contribution of small, compact galaxies to the counts increases faster than that of large galaxies going to faint apparent magnitudes as shown by the steeper slopes derived. It is worth noting that the counts of small sources follow an Euclidean slope which indicates that either they are very low redshift galaxies, very rapidly evolving or a combination of the two. Finally, Figs. 10, 11 and 12 indicate that small galaxies contribute most to the blue population. *Our conclusion is that sub-L^*_K galaxies contribute to the number counts and with increasing weight to fainter magnitudes.*

At faint apparent magnitudes we are sampling the faint-end tail of the local luminosity function superposed on the bright tail ($M_K \leq M^*_K$) of the high redshift galaxy population. The relative contribution to the total number of galaxies at a given apparent magnitude depends on the volume sampled by a given luminosity and on the density of galaxies with that luminosity. A large contribution to faint counts could come from the faint end of the LF in the case of a steep slope ($\alpha < -1$) since the number of luminous galaxies would increase slower than that of the intrinsically faint ones at faint apparent magnitudes. In this case we should first observe a reddening trend of the J-K color due to the rapid increase of galaxies with progressively higher redshift going to fainter apparent magnitudes. Such a trend would be expected to continue steadily as long as the number of intrinsically faint galaxies, and hence low redshift galaxies, starts to increase more rapidly than high-z galaxies. The mean observed color should therefore become increasingly bluer, contrary to what is expected for the standard case of a normal high-z galaxy population. Moreover, the median redshift would increase more slowly than expected going to fainter apparent magnitudes, as observed by Cowie et al. (1996) in their redshift survey.

For example, assuming a slope $\alpha = -1.6$ at luminosities $L < 0.01L^*$, as in the ESP (Zucca et al. 1997), by integrating the LF down to $0.0001L^*$ we find that more than 40% of the galaxies in the magnitude range $21 < K < 22$ are at $z < 0.5$ and more than 60% at $z < 1$. These fractions could even increase to 60% and 80% in the case of a steeper LF, for example according to the result of Marzke et al. (1994, 1998) or De Propris et al. (1998a), or integrating the LF down to a fainter cutoff. It is worth noting that this simple scenario, which is a straightforward consequence of a steepening trend in the LF faint-end tail, would also account for the observed trend in galaxy size and compactness parameter, as discussed earlier. Assuming that faint galaxies are actually intrinsically faint IR objects and that the IR luminosity is also a fair tracer of mass (Gavazzi et al. 1996) implies that compact systems of low mass constitute an important population in the Universe at least back to $z \sim 1$.

7. Summary, conclusions and future work

We have presented counts, colors and sizes of galaxies detected in deep J (down to J=24) and Ks (down to Ks=22.5) images obtained with the new IR imager/spectrometer SOFI at the ESO NTT telescope. These data represent the largest samples collected so far reaching these depths. The main results obtained from analysis of the data are the following:

- number counts follow a $d\ log(N)/dm$ relation with slope 0.38 in Ks and 0.36 in J showing no sign of any flattening or turnover down to the faintest magnitudes. This fully agrees with most of the previous ground-based data and with the deepest NICMOS/HST data;
- fainter than Ks~ 19 and J~ 20, the median J-K galaxy color shows a break in its reddening trend and turns toward bluer colors;
- faint bluer galaxies display both a larger compactness index and smaller apparent sizes;
- the J-K color distribution of small and of large galaxies (selected with respect to the median size of the whole sample) are significantly different with small galaxies contributing most to the blue population;
- the number counts of small galaxies follow an Euclidean slope, much steeper than that of large sources, and dominate the deep number counts fainter than Ks=21.5 and J=23.

The absence of a turnover in the counts down to the faintest magnitudes is indicative of an increasing contribution of sub-L* and thus low redshift galaxies ($z < 1$) leading to envisage a sub-

[2] In a recent paper Im et al. (1999) present a morphologically divided redshift distribution of a sample of galaxies limited to I=21.5. They argue that the faint end slope of the LF of very late type galaxies should be steeper than $\alpha = -1.4$

stantial steepening in the faint-end tail of the galaxy LF. Such a claim is also supported by the observed color trend which seems to rule out any major contribution of high-z galaxies as primary contributors to faint counts. Moreover also the Euclidean slope shown by counts of small galaxies supports this claim. In particular the Euclidean slope indicates that either small galaxies are at very low redshift, or that they are very rapidly evolving or a combination of the two.

The existence of a steep ($\alpha \ll -1$) faint-end tail ($L < 0.1$–$0.01L^*$) in the IR LF would naturally account both for the J-K color trend, the compactness trend and the different slope shown by the counts of small and large galaxies, the former being described by a much steeper (nearly Euclidean) slope.

Very little is known about the redshift distribution of galaxies to faint K magnitudes. Two spectroscopic surveys, Cowie et al. (1996) and Cohen et al. (1999) based on a K=20 limited sample have been carried out so far. Taking into account their redshift incompleteness, it seems that 10–30% of objects are at $z > 1$. The population we are discussing here is concentrated at K> 20. It will prove quite difficult to obtain spectroscopic redshifts for these objects since their R magnitudes should be fainter than 24 and obtaining IR spectra would be equally difficult even using an IR spectrometer like ISAAC at the VLT. The most promising approach to understand the properties of the faint population is the use of photometric redshifts based on color measurements from the U to K bands (Fontana et al. 1999a; Benitez et al. 1999). This is already being done on the SUSI NTT Deep Field, a subsection of the area covered by the images analyzed in this paper (Arnouts et al. 1999; Fontana et al. 1999b).

Acknowledgements. We wish to thank the referee, M. Bershady, for the valuable comments and suggestions which significantly improved the manuscript. The authors are grateful to N. Devillard for his valuable help in the data reduction and P. A. Duc for providing support in the astrometric calibration. PS is grateful to A. Iovino and G. Chincarini for helpful discussions and their suggestions.

References

Abraham R.G., Valdes F., Yee H. K.C., van den Bergh S., 1994, ApJ 432, 75
Abraham R.G., van den Bergh S., Ellis R.S., et al., 1996, ApJS 107, 1
Arnouts S., D'Odorico S., Cristiani S., et al., 1999, A&A 341, 641
Avni Y., Soltan A., Tanambaum H., Zamorani G., 1980, ApJ 235, 694
Babul A., Rees M., 1992, MNRAS 255, 346
Benitez N., Broadhurst T., Bouwens R., Silk J., Rosati P., 1999, ApJ 515, L65
Bernstein G.M., Nichol R.C., Tyson J.A., Ulmer M.P., Wittman D., 1995, AJ 110, 1507
Bershady M.A., Lowenthal J.D., Koo D.C., 1998, ApJ 505, 50
Bershady M.A., Subbarao M., Koo D.C., Szalay A., Kron R.G., 1999, in preparation
Bertin E., Arnouts, S., 1996, A&AS 117, 393
Brainerd T.G., Smail I.R., Mould J.R., 1994, BAAS 185, 114.06
Brinchmann J., Abraham R., Schade D., et al., 1998, ApJ 499, 112
Broadhurst T.J., Ellis R.S., Glazebrook K., 1992, Nat 355, 55
Buzzoni A., 1989, ApJS 71, 817
Buzzoni A., 1995, ApJS 98, 69
Buzzoni A., 1998, ApJ submitted
Buzzoni A., 1999, MNRAS submitted
Carlberg R.G., Cowie L.L., Songaila A., Hu E.M., 1997, ApJ 484, 538
Cohen J.G., Blandford R., Hogg D.W., Pahre M.A., Shopbell P.L., 1999, ApJ 512, 30
Colless M., Schade D., Broadhurst T.J., Ellis R.S., 1994, MNRAS 267, 1108
Cowie L.L., Gardner J.P., Lilly S.J., McLean I., 1990, ApJ 360, L1
Cowie L.L., Gardner J.P., Hu E.M., et al., 1994, ApJ 434, 114
Cowie L.L., Songaila A., Hu E.M., Cohen J.G., 1996, AJ 112, 839
De Propris R., Eisenhardt P.R., Stanford S.A., Dickinson M., 1998a, ApJ 503
De Propris R., Pritchet C.J., 1998b, AJ 116, 1118
Driver S.P., Phillips S., Davies J.I., Morgan I., Disney M.J., 1994, MNRAS 268, 393
Driver S.P., Windhorst R.A., Griffiths R.E., 1995, 453, 48
Djorgovski S., Spinrad H., 1981, ApJ 251, 417
Djorgovski S., Soifer B.T., Pahre M., et al., 1995, ApJ 438, L13
Efstathiou G., Ellis R.S., Peterson B.A., 1988, MNRAS 232, 431
Feigelson E.D., Nelson P.I., 1985, ApJ 293, 192
Ferreras I., Cayon L., Martinez-Gonzalez E., Benitez N., 1998, MNRAS 304, 319
Fontana A., D'Odorico S., Fostbuty R., et al., 1999a, A&A, in press (astro-ph/9901359)
Fontana A., Menci N., D'Odorico S., et al., 1999b, MNRAS, in press
Gardner J.P., Cowie L.L., Wainscoat R.J., 1993, ApJ 415, L9
Gardner J.P., Sharples M.R., Frenk C.S., Carrasco B.E., 1997, ApJ 480, L99
Gavazzi G., Pierini D., Boselli A., 1996, A&A 312, 397
Glazebrook K., Peacock J., Collins C., Miller L., 1994, MNRAS 266, 65
Glazebrook K., Ellis R., Santiago B., Griffiths R., 1995a, MNRAS 275, L19
Glazebrook K., Peacock J., Miller L., Collins C., 1995b, MNRAS 275, 169
Gronwall C., Koo D.C., 1995, ApJ 440, L1
Im M., Griffiths R.E., Naim A., et al., 1999, ApJ 510, 82
Isobe T., Feigelson E.D., Nelson P.I., 1986, ApJ 306, 490
Kron R.G., 1980, ApJS 43, 305
Kron R.G., 1995, In: Sandage A.R., Kron R.G., Longair M.S. (eds.) The Deep Universe. Springer
Lilly S.J., Cowie L.L., Gardner J.P., 1991, ApJ 369, 79
Lilly S.J., Tresse L., Hammer F., Crampton D., Le Fevre O., 1995, ApJ 455, 108
Liu C.T., Green R.F., Hall P.B., Osmer P.S., 1998, AJ 116, 1082
Lobo C., Biviano A., Durret F., et al., 1997, A&A 317, 385
Marzke R.O., Geller M.J., Huchra J.P., Corvin H.G., 1994, AJ 108, 437
Marzke R.O., Da Costa L.N., 1997, AJ 113, 1
Marzke R.O., Da Costa L.N., Pellegrini P.S., Willmer C.N.A., Geller M.J., 1998, 503, 617
McCracken H.J., Metcalfe N., Shanks T., et al., 1999, MNRAS, astro-ph/9904014
McLeod B.A., Bernstein G.M., Reike M.J., Tollestrup E.V., Fazio G.G., 1995, ApJS 96, 117
Metcalfe N., Shanks T., Fong R., Roche N., 1995, MNRAS 273, 257
Minezaki T., Kobayashi Y., Yoshii Y., Peterson B.A., 1998, ApJ 494, 111
Mobasher B., Sharples R.M., Ellis R.B., 1993, MNRAS 263, 560
Mobasher B., Trentham N.D., 1998, MNRAS 293, 315
Molinari E., Chincarini G., Moretti A., De Grandi S., 1998, A&A 338, 874
Moorwood A., Cuby J.G., Lidman C., 1998, The Messenger 91, 9

Moustakas L.A., Davis M., Graham J.R., et al., 1997, ApJ 475, 445
Persson E., Murphy D.C., Krzeminski W., Roth M., Rieke M.J., 1998, AJ 166, 2475
Petrosian V., 1976, ApJ 210, L53
Petrosian V., 1998, (astro-ph/9807189)
Roche N., Eales S., Hippelein H., 1998, MNRAS 295, 946
Roche N., Shanks T., Metcalfe N., Fong R., 1996, MNRAS 280, 397
Saracco P., Iovino A., Garilli B., Maccagni D., Chincarini G., 1997, AJ 114, 887
Soifer B.T., Matthews K., Djorgovski S., et al., 1994, ApJ 420, L1
Szokoly G.P., Subbarao M.U., Connolly A.J., Mobasher B., 1998, ApJ 492, 452
Yan L., McArthy P.J., Storrie-Lombardi L.J., Weymann R.J., 1998, ApJ 503, L19
Yoshii Y., Peterson B.A., 1995, ApJ 444, 15
Zucca E., Zamorani G., Vettolani G., et al., 1997, A&A 326, 477